


Diagnosis of 3D magnetic field and modes composition in MHD turbulence with Y-parameter

Sunil Malik ^{1,2} *, Ka Ho Yuen ³ †, Huirong Yan ^{1,2} ‡

¹*Institute für Physik und Astronomie Universität Potsdam, Golm Haus 28, D-14476 Potsdam, Germany*

²*Deutsches Elektronen-Synchrotron DESY, Platanenallee 6, 15738 Zeuthen, Germany*

³*Theoretical Division, Los Alamos National Laboratory, Los Alamos, NM 87545, USA*

Accepted XXX. Received YYY; in original form ZZZ

ABSTRACT

Magnetic fields are crucial in numerous astrophysical processes within the interstellar medium. However, the detailed determination of magnetic field geometry is notoriously challenging. Based on the modern magnetohydrodynamic (MHD) turbulence theory, we introduce a novel statistical technique, the "Y-parameter", to decipher the magnetic field inclination in the ISM and identify dominant turbulence modes. The Y-parameter, calculated as the ratio of anisotropies of different Stokes parameter combinations, displays contrasting trends with the mean-field inclination angle in Alfvénic and compressible turbulence modes. A Y-parameter value around 1.5 ± 0.5 provide a statistical boundary to determine the dominant MHD turbulence modes. We have discovered specific correlations between the Y-parameter value and the inclination angle that unveil the dominant turbulence mode. This methodology, when applied to future radio polarisation surveys such as LOFAR and SKA, promises to significantly enhance our knowledge of 3D magnetic field in the ISM and improve our understanding of interstellar turbulence.

Key words: Synchrotron radiation, magnetic fields – polarization, Stokes parameters, general – interstellar medium – techniques: Astrophysical Plasma turbulence

1 INTRODUCTION

The ISM is a complex, multi-phase environment comprising of gas, dust, and magnetic fields. Its magnetized and turbulent nature provides us with a good environment to study the magnetohydrodynamic (MHD) turbulence in our galaxy (Armstrong et al. 1995; Elmegreen & Scalo 2004; Boldyrev 2006; McKee & Ostriker 2007; Draine 2011). MHD turbulence is important for a wide range of astrophysical processes, such as the formation and evolution of stars, the transport of energy and momentum, cosmic ray scattering and acceleration (Jokipii 1966; Lerche & Schlickeiser 2001; Qin et al. 2002; Yan & Lazarian 2002, 2008a; Yan et al. 2008; Yan 2022; Lemoine 2022; Sampson et al. 2023) and the amplification of magnetic fields (Lazarian et al. 2020). Observational detection of the properties of MHD turbulence in the ISM is essential for a comprehensive understanding of the latter and the processes that take place within it.

The 3D inclination of the magnetic field in interstellar media and its relation to other physical processes is one of the most important scientific questions in the astrophysical community. However, determining the properties of the magnetic field, in particular, its interplay with the ubiquitous interstellar turbulence, is notoriously difficult. Measurement of magnetic field properties mainly relies on two popular observational techniques: polarimetry from synchrotron radiation

or dust emission/absorption that only gives the line-integrated or plane of sky magnetic field direction (Davis & Greenstein 1951; Hildebrand 2002; Lazarian & Hoang 2007; Andersson et al. 2015; Hensley et al. 2019), and Zeeman splitting that gives line-of-sight magnetic field strength in dense clouds (Crutcher 1999; Chepurnov et al. 2010). Recent effort based on atomic alignment in the magnetic field suggests that the 3D magnetic field topology in the diffuse medium could possibly be measured (Yan & Lazarian 2006; Kuhn et al. 2007; Yan & Lazarian 2007, 2008b, 2012), but currently restricted to metal absorption lines due to instrumental restrictions (Zhang et al. 2020b). Therefore, the search for the 3D magnetic field and its underlying relation to turbulence is in a deadlock.

Similar problems happen also for the determination of the nature of MHD turbulence, e.g. sonic and Alfvénic Mach number or MHD mode fractions, in observational data. Several efforts have been made in retrieving the essential parameters in ISM turbulence observations through statistical techniques. One common method is to measure the power spectrum of electron density fluctuations in the ISM (Armstrong et al. 1995; Chepurnov & Lazarian 2010), which can reveal the presence of turbulent motions. Other methods include studying the velocity statistics in the ISM using spectroscopic observations (Lazarian et al. 2004), and mapping the distribution of magnetic fields using polarization or spectroscopic measurements (e.g. Heyer et al. 2008). Despite that, the measurement in earlier studies is either based on crude models of turbulence statistics or qualitative relations between different turbulence observables.

Recent theoretical developments on magnetized turbulence theory suggest that the properties of the magnetic field are encoded in

*E-mail: sunil.malik@uni-potsdam.de (SM)

†kyuen@lanl.gov (KHY)

‡huirong.yan@desy.de (HY) (Corresponding Author)

the statistics of MHD turbulence (Yan & Lazarian 2004; Lazarian & Pogosyan 2012; Makwana & Yan 2020). Conceptually, MHD turbulence can primarily be decomposed into three modes: Alfvén mode, the fast and slow magnetosonic modes (also known as magneto-acoustic modes) (Cho & Lazarian 2003). Magnetic field lines are stretched differently by Alfvén and magnetosonic modes, and therefore the statistics of magnetic field observables are different. Utilizing this fact, Zhang et al. (2020a) and later Yuen et al. (2023) suggest that the statistics of polarized synchrotron radiation reflect the fluctuations in the embedded magnetic fields caused by turbulence, which in turn allows us to study the magnetic field and its turbulent properties. In this paper, we aim to develop a new statistical recipe to retrieve the magnetic field inclination angle and the properties of underlying MHD turbulence using simulated datacubes.

The structure of the paper is as follows. In §2, we discuss our theoretical construction in measuring the line of sight angle from the theory of turbulence statistics. The numerical simulation setup and its observables are described in §3. Our detailed analysis and decomposed and total cubes results can be found in §4. We discuss the impact of our results in §5, and we conclude our paper at §6.

2 THE ESSENCE OF THE Y-PARAMETER ANALYSIS

2.1 Mapping theory of turbulence statistics and their discrepancies

Let us first briefly summarize the “Y-parameter” analysis proposed in Yuen et al. (2023). The fundamental question that statistical theory of MHD turbulence based on the axis-symmetric assumption (Monin & I’Aglom 1971; Shivamoggi 1999; Lazarian & Pogosyan 2000, Yan & Lazarian 2002, Haugen et al. 2004; Müller & Grappin 2005; Galtier 2009; Banerjee & Galtier 2013; Yuen et al. 2021) wants to resolve is “how observational statistics are mapped from the 3D turbulence statistics”. These series of works usually assume a given statistics of 3D turbulence variables (i.e., 3D density (ρ), 3D turbulence velocity (\mathbf{v}) and magnetic field (\mathbf{B})) in the form of spectral slopes (Armstrong et al. 1995; Chepurnov et al. 2010), anisotropy measure (Cho & Lazarian 2002, 2003; Müller & Grappin 2005; Esquivel & Lazarian 2005) and tensor structures (Yan & Lazarian 2002; Banerjee & Galtier 2013; Verdini et al. 2015; Kandel et al. 2016, 2017; Zhang et al. 2020a). The mapping of the 3D statistics to observable statistics is highly nontrivial in interferometry (Lazarian & Pogosyan 2000; Yuen et al. 2021) and polarimetry (Lazarian & Pogosyan 2012, 2016). Notably, both line of sight angles and energy fraction of MHD modes are stored non-linearly in observables’ statistics (i.e., spectrum, anisotropy, and tensors).

Attempts have been made to retrieve the line of sight angles and mode fraction from observational data. For instance, earlier attempts asserted that the line of sight angles could be estimated by inspection of polarization percentages (Clark 2018). However, these methods are subjected to strong nonlinear interference from “3D \rightarrow observable” projection, and therefore the accuracy of these methods is questionable. In parallel, the *qualitative* analysis of mode fraction has been proposed by Zhang et al. (2020a), yet there are currently no ways to retrieve the actual quantitative fraction of MHD modes in observations.

2.2 Y-parameter Science

Recently, based on the “mapping theory” of MHD turbulence statistics (Lazarian & Pogosyan 2012, 2016), Yuen et al. (2023) pro-

posed a method to retrieve both line of sight angle θ_l and mode fraction concurrently via inspection of observable statistics, namely “Y-parameter analysis”. Suppose X is a 2D observable, then D_X represents the global correlation function (CF) of the observable X :

$$D_X(\mathbf{R}) = \langle (X(\mathbf{R}')X(\mathbf{R}' + \mathbf{R}))^2 \rangle_{\mathbf{R}'} \quad (1)$$

where one can always write $D_X(\mathbf{R}) = D_X(R, \phi)$ via series of multipoles (c.f. Kandel et al. 2016):

$$D_X(R, \phi) = \sum_{m=0,2,4,\dots}^{\infty} D_m(R) \cos(m\phi) \quad (2)$$

where the odd terms of m are zero due to D_X being even. The mapping theory (Lazarian & Pogosyan 2000, 2012, 2016) assumes that the quadrupole-to-monopole ratio (D_4/D_0) and higher order terms are small, which as a result θ_l at most quadratic in the statistics of D_X . This assumption was used in the previous analyses of anisotropy-related methods (e.g. Lazarian et al. 2022). However, the appendix of Yuen et al. (2023) showed that in the case of small Alfvénic Mach Number M_A , none of $D_{m \geq 4}/D_0$ is vanishing, raising concerns about whether studying the statistics of D_2 is sufficient in describing the full fluctuations of observables. Yuen et al. (2023) pointed out that the two-point statistics of observables originating from the same turbulence region carry the same spectrum and anisotropy factors. For instance, Stokes parameters in the case of synchrotron emissions are mostly coming from combinations of magnetic fields, whose statistics are derived from the complete functional forms of spectral, anisotropy, and tensor functions (c.f. Yan & Lazarian 2002; Yuen et al. 2023). Distinct Stokes parameters typically possess identical spectral indices and anisotropy scaling; however, their tensor functions, which depend on the line-of-sight angle, have varying forms. Consequently, the observed statistics of Stokes Q and U, for instance, exhibit differences. Since we usually consider second-order statistics, the tensor functions are at most second order (see, e.g. Lazarian & Pogosyan 2000). As a result, the fraction of two-point statistics from two observables will be at most quadratic of θ_l .

Based on the principles mentioned above, Yuen et al. (2023) suggests that the following parameter

$$Y = \frac{\text{Anisotropy}(D_{I+Q})}{\text{Anisotropy}(D_{I-Q})} = \frac{v/h(D_{I+Q})}{v/h(D_{I-Q})} \quad (3)$$

is a measure of line of sight angle θ_l and mode fraction. Where v and h indicate the length in the vertical and horizontal directions with respect to the plane of sky B-field. This Y-parameter is used in the remainder paper.

3 METHOD

3.1 Numerical simulations

In this paper, we employed two publicly available MHD codes ZEUS-MP/3D (Hayes et al. 2006) and Athena++ (Stone et al. 2020) in simulating magnetized turbulence with different physical conditions. We run our simulations for at least two sound crossing times ($\tau_s = L_{\text{box}}/c_s$). Our data cubes are time series of three-dimensional, triply periodic, isothermal MHD simulations with continuous force driving via OrNSTein-Uhlenbeck forcing, where the smoothing is controlled by $t_{\text{corr}} = 0.01\tau_s$. The energy injection rate is adjusted to simulate various Alfvénic Mach numbers, M_A , and plasma β . The injection is performed so that we only have eddies injected with scales $L_{\text{inj}}/L_{\text{box}} \geq 1/2$, which corresponds to $0 \leq |\mathbf{k}| \leq 2$. The driving force

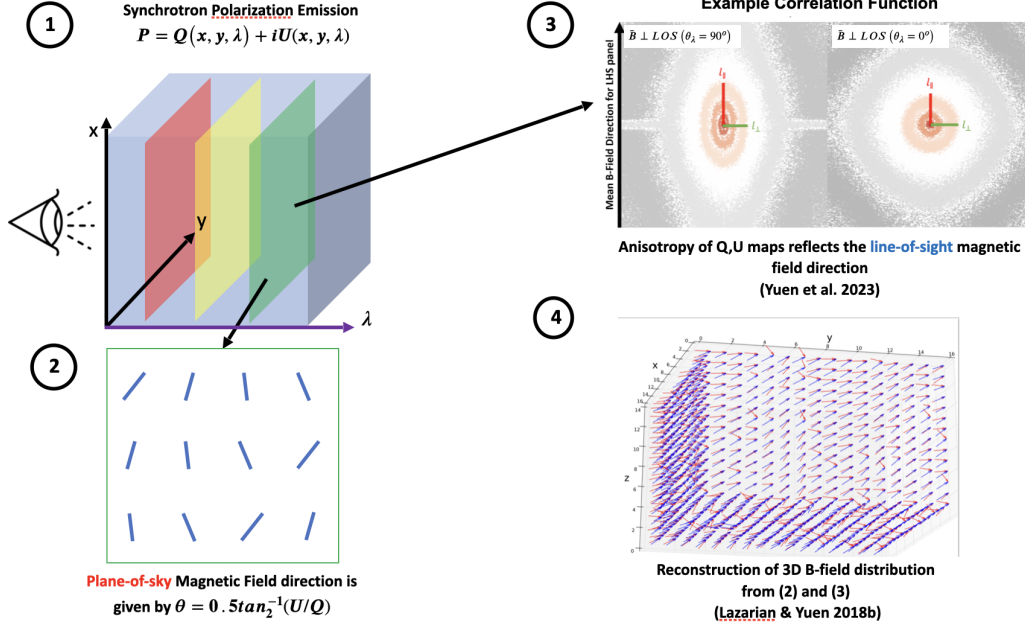


Figure 1. A figure showing how polarized synchrotron emissions store the information of 3D magnetic field. Panel (1): Emissions from synchrotron emission are stored in a spectral-spatial 3D cube $P = P(x, y, \lambda)$, where the 3rd axis is in the unit of wavelength, along the line of sight. (2) For each λ , the magnetic field direction is stored in the synchrotron polarization angle (3) The anisotropy of Stokes parameters stores the information of the magnetic field inclination. (4) With all this information combined, the 3D magnetic field angle can therefore be reconstructed with appropriate mathematical procedures.

contains both incompressible and compressible driving controlled by a free parameter ζ (see Makwana & Yan 2020):

$$\mathbf{f} = \mathbf{f}_{incomp}\zeta + \mathbf{f}_{comp}(1 - \zeta) \quad (4)$$

where $\nabla \cdot \mathbf{f}_{incomp} = 0$. A summary of the simulation parameters is given in Table 1. In our calculations, all physical parameters are set to unity unless specified. Notice that isothermal simulations are scale-free, and so units are not an issue in our calculation.

3.2 Synthesis of synchrotron polarization observables

In general, the synchrotron emission depends on the distribution of relativistic electrons as

$$N_e(\mathcal{E})d\mathcal{E} \sim \mathcal{E}^\alpha d\mathcal{E}, \quad (5)$$

with the intensity of the synchrotron emission being

$$I_{sync}(\mathbf{X}) \propto \int dz B_\perp^\eta(\mathbf{x}) \quad (6)$$

where $\mathbf{X} = (x, y)$ is the 2D position of the sky (POS) vector and $B_\perp = \sqrt{B_x^2 + B_y^2}$ being the magnitude of the magnetic field perpendicular to the line of sight in z -direction. In general, $\eta = 0.5(\alpha + 1)$ is a fractional power law. The statistics of $I(\alpha)$ are similar to that of $I(\alpha = 3)$ (Lazarian & Pogosyan 2012; Zhang et al. 2020a). Therefore, it suffices to discuss the statistical properties of the case $\alpha = 3$.

Per Lazarian & Pogosyan (2012), synchrotron complex polarization function with Faraday rotation is given by:

$$P_{synch}(\mathbf{R}) = \int dz \epsilon_{synch} \rho_{rel} B^2 e^{2i(\theta(\mathbf{R}, z) + C \lambda^2 \Phi(\mathbf{R}, z))} \quad (7)$$

where ϵ_{synch} is the emissivity of synchrotron radiation,

$$\Phi(\mathbf{R}, z) = \int_0^z dz' (4\pi)^{-1/2} \rho_{thermal}(\mathbf{R}, z') B_z(\mathbf{R}, z') \text{rad m}^{-2} \quad (8)$$

is the Faraday Rotation Measure¹. Notice that ρ_{rel} is the relativistic electron density, while $\rho_{thermal}$ is the thermal electron density. The C-factor ≈ 0.81 (Lazarian et al. 2017; Malik et al. 2020). The projected magnetic field orientation is then given by:

$$\theta_B = \frac{\pi}{2} + \frac{1}{2} \tan_2^{-1}\left(\frac{U}{Q}\right) \quad (9)$$

where \tan_2^{-1} is the 2-argument arc-tangent function. Also, we will consider only the statistics of $\eta = 2$ (i.e. $\alpha = 3$).

3.3 Mode fraction analysis

The MHD mode wave-vectors in the case of isothermal MHD are given by (Cho & Lazarian 2003):

$$\begin{aligned} \zeta_A(\hat{\mathbf{k}}, \hat{\lambda}) &\propto \hat{\mathbf{k}} \times \hat{\lambda} \\ \zeta_S(\hat{\mathbf{k}}, \hat{\lambda}) &\propto (-1 + \alpha - \sqrt{D})(\mathbf{k} \cdot \hat{\lambda})\hat{\lambda} \\ &\quad + (1 + \alpha - \sqrt{D})(\hat{\lambda} \times (\mathbf{k} \times \hat{\lambda})) \\ \zeta_F(\hat{\mathbf{k}}, \hat{\lambda}) &\propto (-1 + \alpha + \sqrt{D})(\mathbf{k} \cdot \hat{\lambda})\hat{\lambda} \\ &\quad + (1 + \alpha + \sqrt{D})(\hat{\lambda} \times (\mathbf{k} \times \hat{\lambda})) \end{aligned} \quad (10)$$

where $\alpha = \beta\Gamma/2$, $D = (1 + \alpha)^2 - 4\alpha \cos^2 \theta_\lambda$, $\cos \theta_\lambda = \hat{\mathbf{k}} \cdot \hat{\lambda}$, plasma $\beta \equiv P_{gas}/P_{mag}$ measures the compressibility and $\Gamma = \partial P/\partial \rho$ is the polytropic index of the adiabatic equation of state. The presence of $\hat{\mathbf{k}}$ suggests that the direction of the three mode vectors are changing as \mathbf{k} changes. In this scenario, the perturbed quantities, say for the velocity fluctuations $\mathbf{v}_1 = \mathbf{v} - \langle \mathbf{v} \rangle$ can be written as:

$$\mathbf{v}_1(\mathbf{r}) = \int d^3 \mathbf{k} e^{i\mathbf{k} \cdot \mathbf{r}} \sum_{X \in A, S, F} F_{0,X}(\mathbf{k}) F_{1,X}(\mathbf{k}, \hat{\lambda}) C_X \zeta_X(\hat{\mathbf{k}}, \hat{\lambda}) \quad (11)$$

¹ It is usually more convenient to use $H_z = B_z/\sqrt{4\pi}$ for analysis.

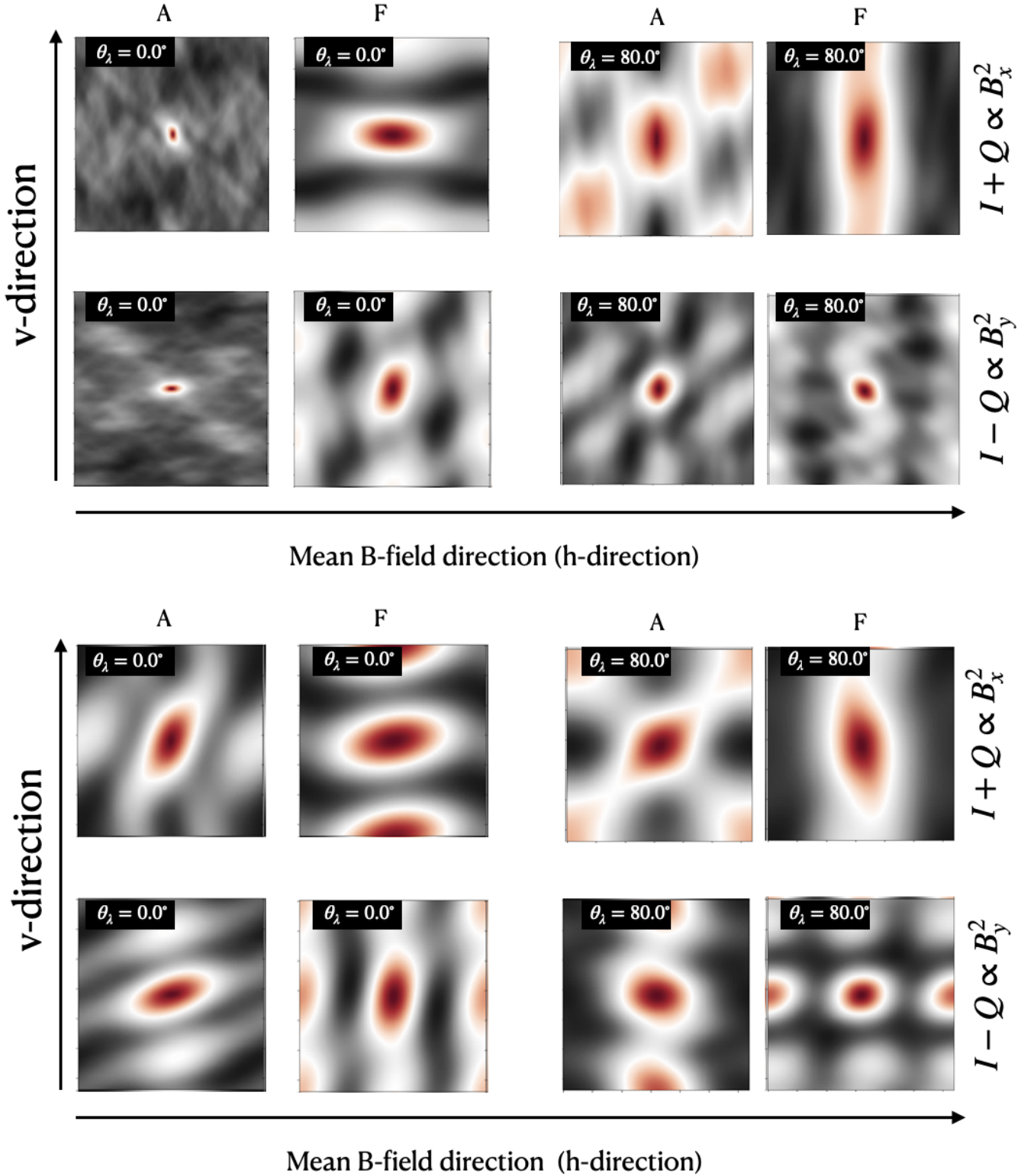


Figure 2. *Upper panel:* The figure shows the correlation function of the decomposed plane of sky components of \mathbf{B} field (B_x , B_y) of the A (Alfvén) and F (compressible) modes for the solenoidal forcing Z12 MHD data cube with $M_A \sim 0.26$ and $\beta \sim 0.12$ at two θ_λ values. The upper and lower sub-panels are for B_x^2 and B_y^2 , respectively. *Lower panel:* same as an upper panel but for the compressible forcing Athena++ A1 cube with $M_A \sim 0.09$. The mode decomposition is performed using the PCA decomposition method described in (Lazarian & Pogosyan 2012).

Model Name	Code	Sonic	Alfvénic	Plasma	Energy	Resolution	C-Mode
		Mach	Mach	Beta	Injection		Energy
		Number	Number		Rate		Fraction
		M_S	M_A	β	ϵ	N_x	f_C
AS7	Athena++	1.47	0.30	0.08	1.0	512	0.18
Z15	ZEUS-MP	2.13	0.52	0.12	0.1	512	0.24
Z12	ZEUS-MP	1.06	0.26	0.12	0.01	512	0.24
AS5	Athena++	1.43	0.29	0.08	1.0	512	0.27
AS6	Athena++	0.29	0.13	0.40	0.1	512	0.30
AS3	Athena++	1.40	0.29	0.08	1.0	512	0.32
AS4	Athena++	0.28	0.13	0.45	0.1	512	0.33
Z8	ZEUS-MP	0.44	0.45	2.06	0.001	512	0.34
Z9	ZEUS-MP	0.45	0.11	0.12	0.001	512	0.35
AS1	Athena++	1.33	0.27	0.08	1.0	512	0.35
Z11	ZEUS-MP	0.93	0.99	2.28	0.01	512	0.36
Z5	ZEUS-MP	0.15	0.15	2.00	0.0001	512	0.39
AS2	Athena++	0.26	0.12	0.42	0.1	512	0.41
Z4	ZEUS-MP	0.15	0.61	32.88	0.0001	512	0.44
A7	Athena++	0.18	0.10	0.61	0.1	512	0.44
A9	Athena++	0.18	0.10	6.47	0.1	512	0.45
Z6	ZEUS-MP	0.14	0.04	0.13	0.0001	512	0.49
A8	Athena++	0.03	0.04	3.55	0.01	512	0.50
A10	Athena++	0.03	0.04	3.55	0.01	512	0.51
A5	Athena++	0.17	0.10	0.69	0.1	512	0.58
A6	Athena++	0.03	0.04	3.55	0.01	512	0.59
A3	Athena++	0.15	0.09	0.72	0.1	512	0.66
A4	Athena++	0.02	0.04	8.00	0.01	512	0.75
A1	Athena++	0.13	0.09	0.95	0.1	512	0.84
A2	Athena++	0.02	0.03	4.50	0.01	512	0.91

Table 1. This table contains all the properties of numerical simulations used in the analysis, sorted according to the Compressible mode (C-Mode) Energy Fraction. The cubes with ‘Z’ and ‘AS’ model names are simulated with Zeus and Athena++ solenoidal forcing, whereas the datacubes with ‘A’ model names are generated with Athena++ compressible forcing.

where C_X denotes the relative weight of the modes and F_0 , F_1 represents the power spectrum, and anisotropy weight, respectively (see Yuen et al. 2023 and refs therein). The “magnetic field frame”, which we will not cover in this paper, is given by an additional rotation of $\tan \theta_\lambda$ from the P(otential)-C(ompressible)-A(lfvén) frame ($\hat{\zeta}_P = \hat{\mathbf{k}}$, $\hat{\zeta}_A = \hat{\mathbf{k}} \times \hat{\lambda}$, $\hat{\zeta}_C = \hat{\mathbf{k}} \times (\hat{\mathbf{k}} \times \hat{\lambda})$). The PCA frame has its special advantage since the \mathbf{k} sampling is usually complete in $d\Omega_k$. Therefore, we can fix \mathbf{k} despite other unit vectors changing. For ζ_x , We can always write the arbitrary vector in the Fourier space as :

$$\zeta_i(\mathbf{k}) = C_P \hat{k}_i + C_C \frac{(\hat{\mathbf{k}} \times (\hat{\mathbf{k}} \times \hat{\lambda}))_i}{|\hat{\mathbf{k}} \times \hat{\lambda}|} + C_A \frac{(\hat{\mathbf{k}} \times \hat{\lambda})_i}{|\hat{\mathbf{k}} \times \hat{\lambda}|} \quad (12)$$

which we will name the unit vector $\zeta_{P,C,A}$.

3.4 Rotation algorithm

In this paper, we adopt the Euler rotation algorithm² that is adopted in Lazarian et al. (2018) & Lazarian et al. (2022) for obtaining numerical cubes with mean magnetic field at different inclination angle, θ_λ . The rotation algorithm in the case of triply periodic numerical cubes has issues in double-counting the corners, which creates artificial effects, especially on the mean of Stokes parameters near $\theta_\lambda \approx \pi/4$. To mitigate the effect, one can introduce a spherical filter positioned at the center of the cube. The spherical filter ensures that the basic statistics of Stokes parameters stay regular. For our study, we emphasize that the application of spherical filter does not change

the scale-dependent anisotropy of the Stokes parameters correlation function. The rotation matrices are defined as :

$$\begin{aligned} \hat{\mathbf{T}}_x &= \begin{bmatrix} 1 & 0 & 0 \\ 0 & \cos(\theta_x) & -\sin(\theta_x) \\ 0 & \sin(\theta_x) & \cos(\theta_x) \end{bmatrix} \\ \hat{\mathbf{T}}_y &= \begin{bmatrix} \cos(\theta_y) & 0 & \sin(\theta_y) \\ 0 & 1 & 0 \\ -\sin(\theta_y) & 0 & \cos(\theta_y) \end{bmatrix} \\ \hat{\mathbf{T}}_z &= \begin{bmatrix} \cos(\theta_z) & -\sin(\theta_z) & 0 \\ \sin(\theta_z) & \cos(\theta_z) & 0 \\ 0 & 0 & 1 \end{bmatrix} \end{aligned} \quad (13)$$

where we will write the rotation matrix $\hat{\mathbf{T}} = \hat{\mathbf{T}}_x \hat{\mathbf{T}}_y \hat{\mathbf{T}}_z$ and $\theta_{x,y,z}$ are desired rotations along the x,y,z axis respectively.

For rotations of 3D scalar cubes, say $\rho(\mathbf{r})$ with $\mathbf{r} \in \mathcal{R}^3$, the new cube is given by $\rho(\hat{\mathbf{T}}^{-1}\mathbf{r})$. For vector cubes $\mathbf{x}(\mathbf{r})$, the new cube is given by $\hat{\mathbf{T}}\mathbf{x}(\hat{\mathbf{T}}^{-1}\mathbf{r})$. The inverse transform is invoked for the position vector \mathbf{r} because the rotation of cubes is equivalent to rotating the observing frame in the opposite direction.

4 ANALYSIS AND RESULTS

To establish the Y-parameter as a reliable technique, we test this method to numerical MHD cubes with various plasma properties, as outlined in Table 1. Although ISM compositions can be intricate, we aim to simplify our analysis by focusing on a combination of independent emitting layers and not considering the impact of Faraday rotations, as shown in the first panel of Figure 1. These emit-

² <https://www.github.com/doraemonho/LazRotationDev>

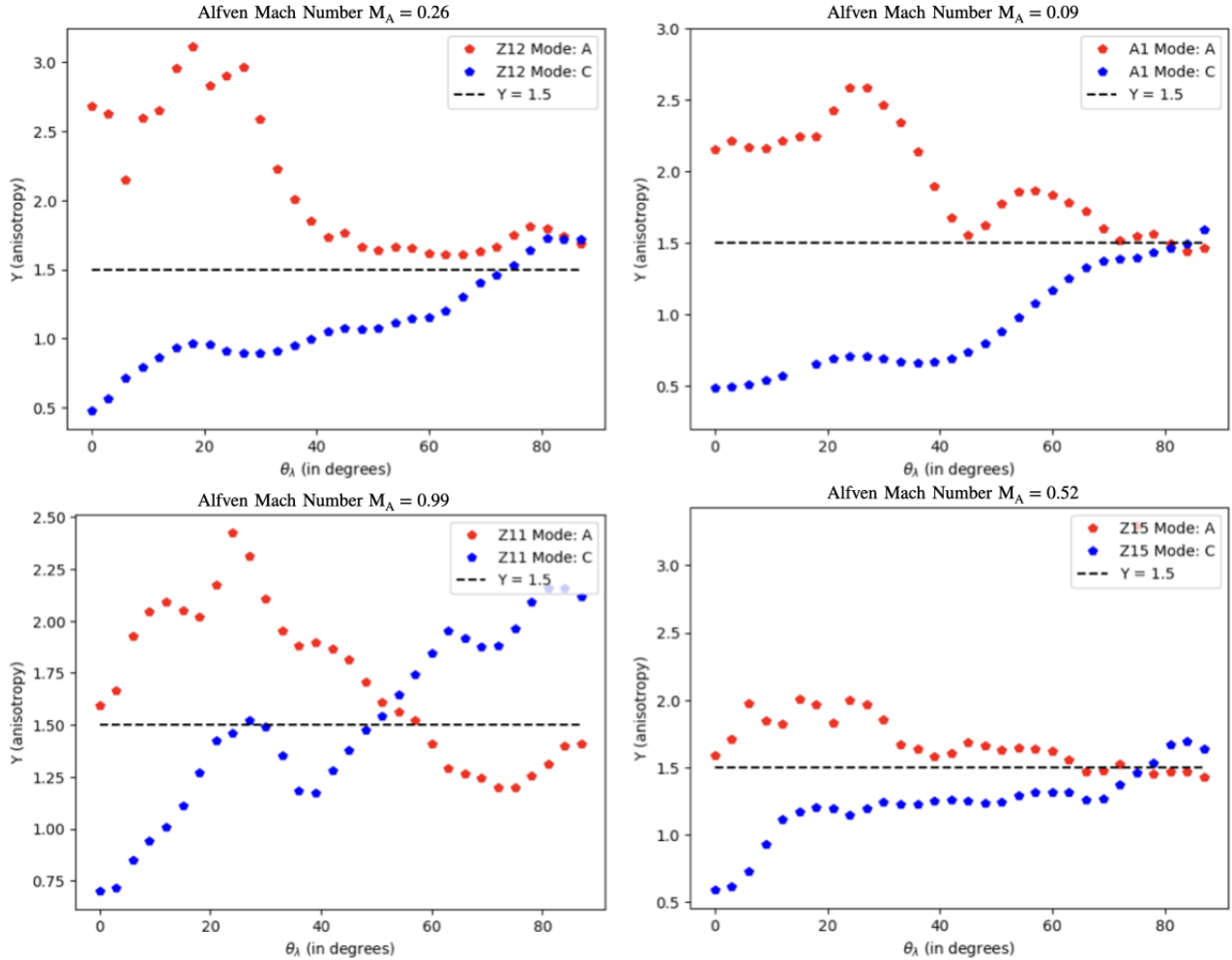


Figure 3. The plots of Y-parameter vs θ_λ for the decomposed \mathbf{B} field: pure A (Alfven mode) and pure C (Compressible mode). The red and blue diamond symbol represents the Alfven and Compressible MHD turbulence modes. Where the black dashed line indicates the $Y \approx 1.5$. We have plotted four panels for datacube with model names Z12, A1, Z11, and Z15 having different turbulence properties. Here datacube A1 is generated with compressible forcing and is predominately composed of compressible modes.

ting layers contain fluctuating small-scale magnetic fields, shown in panel 2 of Figure 1. In addition to these small-scale components, our data cubes exhibit a mean magnetic field since $M_A \lesssim 1$. By analyzing these data cubes, we can gain insight into the nature of MHD turbulence and orientation of B-field in the ISM plasma and further develop our understanding of this important astrophysical phenomenon.

4.1 Analysis of decomposed data cubes

In order to gain a better understanding of the behaviour of the Y-parameter for various MHD turbulent plasma modes and its dependence on θ_λ , we initially decomposed the magnetic fields of our MHD cubes into two general components: Alfven mode (A) and compressible modes (F or C, which we use interchangeably), utilizing the PCA decomposition techniques as briefly described in § 3.3 (see Lazarian & Pogosyan 2012 for more details). We then proceeded to investigate the anisotropies of projected observables $I + Q \propto B_x^2$ and $I - Q \propto B_y^2$ for each of these modes separately. It is worth noting that due to their different dependence on the B_\perp and B_\parallel

components, the anisotropy also inherently depends on θ_λ . To illustrate the variation of anisotropy, we have presented two cases in Figure 2, one with $\theta_\lambda \sim 0.0^\circ$ and another at $\theta_\lambda \sim 80.0^\circ$. The upper panel of Fig. 2 shows the orientation of the correlation functions for both A and F decomposed modes for the solenoidal-forcing Z12 MHD datacube. Meanwhile, the lower panel of Figure 2 shows the correlation function orientations for the compressible-forcing A1 cube.

To calculate the Y-parameter using the correlation function distributions, we adopted a fitting approach in the central region with Gaussian functions along both directions. The presence of a smooth distribution of correlation function contours on the fitting scale is a prerequisite the analysis. By analyzing these figures, we can draw the following conclusions:

- (i) Low θ_λ case: The anisotropy of B_x^2 and B_y^2 for the A mode is perpendicular and parallel to the projected mean magnetic field, respectively. However, it is vice versa for the case of F mode.
- (ii) High θ_λ case: These anisotropies of B_x^2 and B_y^2 are more or less the same irrespective of A and F mode.
- (iii) The relative anisotropies (Eq. 3) for B_x^2 and B_y^2 can give us a parameter that can be used to characterize the MHD turbulence

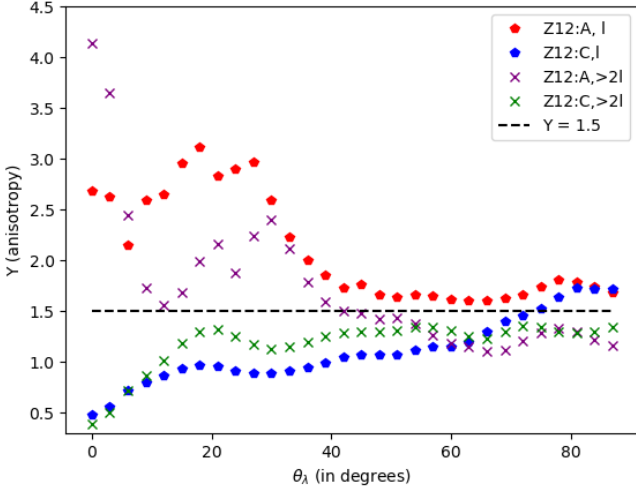


Figure 4. The plot illustrates the variation of the Y-parameter versus θ_λ with length scale. Here, we have computed the Y-parameter for the decomposed B-field at a specific length scale, denoted as ‘ l ’ (indicated by the red and blue diamond symbols for A and C modes). This length scale lies within the injection length scale. Further, we have also evaluated the Y-parameter as a function of θ_λ using a larger length scale of ‘ $2l$ ’ (represented by the purple and green cross symbols for A and C modes), which extends beyond the injection length scale.

modes in the given turbulent media. Due to its dependency on θ_λ , it can be used as a probe to retrieve the mean field inclination angle in ISM.

To investigate the relationship between the Y-parameter and the mean-field inclination angle, θ_λ , we analyzed the Y-parameter for decomposed A and F modes obtained from four distinct MHD turbulence datacubes, as illustrated in Fig.3. Our analysis revealed that the Y-parameters for the A and F modes exhibit different characteristics. Specifically, the Y-parameter for the pure F (compressible) mode shows an increasing trend as θ_λ increases. In contrast, the Y-parameter for the pure A (Alfvén) mode exhibits a decreasing trend with θ_λ . Even though they were generated using different driving mechanisms (the left upper panel of Fig.3 depicts the Z12 cube with solenoidal forcing, while the right upper panel depicts the A1 cube with compressible forcing), the functional dependency of the Y-parameter for pure F and A modes exhibit similar functional dependencies on θ_λ . Notably, the average Y-parameter has clear separation at the value of $Y \sim 1.5$, which could be used as a criterion to distinguish between MHD turbulence modes. Additionally, we would like to highlight that the relative anisotropy, Y-parameter, is estimated through the fitting of the Correlation Function, as depicted in Fig. 2, using length scales that fall within the injection length scale. In Fig. 4, we observe that when the length scale is within the inertial range, the decomposed B-field exhibits contrasting trends in the Y-parameter and converges toward $\sim 1.5 \pm 0.5$ at higher θ_λ . However, for tests using larger length scales that lie outside the inertial range, the Y-parameter began to converge towards the statistical demarcation of $\sim 1.5 \pm 0.5$ even at smaller θ_λ .

To replicate the complex composition of the ISM, we employed the Y-parameter as a mode decomposition technique on 25 datacubes of MHD turbulence ($M_A < 1.0$), spanning a wide range of plasma properties, energy injection rates, and driving mechanisms (see Table 1). While analyzing the individual cubes, we found that the technique gives ambiguous results when the compressible mode energy

fraction of the cubes lies in the range of $0.5 < f_C < 0.6$. Therefore, to ensure the validity of our results, we excluded 5 datacubes with C-mode energy fractions falling between 0.5 and 0.6. The remaining dataset comprised of 12 turbulence cubes subjected to solenoidal forcing, exhibiting less than 40% of energy in the Compressible turbulence mode, and 8 datacubes characterized by compressible-driven turbulence, with a dominating energy fraction in the compressible mode. We investigated the correlation function of B_x^2 and B_y^2 for the individual modes decomposed from all these cubes and found that they follow a similar trend, as shown in Fig.2. Furthermore, we evaluated the relative anisotropies, or “Y-parameter,” for each cube and found an equivalent trend for the Z12 and A1 cubes, as demonstrated in the upper two panels of Fig.3.

To improve the statistical significance of our results, we calculated the statistical probability density and median of the Y-parameter for the A and C modes in their respective decomposed data cubes at every θ_λ value. The probability density (PDF) and median Y-parameter against θ_λ is presented in Fig.5, where the left panel represents the 12 MHD turbulence cubes with $f_C < 0.4$. In contrast, the right panel comprises 8 compressible dominant datacubes with $f_C > 0.5$. The upper and lower sub-panels in Fig.5 show purely Alfvénic and compressible modes, respectively. Notably, the functional dependency of the Y-parameter on θ_λ in both these plots for the Alfvén and compressible modes is consistent with the behaviour of the Y-parameter in the individual data cube. Thus it can act as a powerful diagnostic for the reconstruction of 3D magnetic fields and understand the mode-decomposition of MHD turbulence.

4.2 Analysis of Total Datacube

MHD turbulence in the real scenario is always complex and exhibits a mixture of turbulence modes. To validate our technique for the reconstruction of 3D magnetic fields and to understand the MHD turbulence mode, we investigate the total B-field of 25 datacubes listed in Table 1. We begin by estimating the correlation function of B_x^2 and B_y^2 for the total field and examining their behaviour with respect to θ_λ . The correlation functions of two cubes are plotted in Fig.6. The left panel of this figure shows that the correlation functions for the Z12 MHD cube follow the correlation functions distribution for the decomposed Alfvén mode in the upper panel of Fig.2. Since the Z12 MHD cube is solenoidally driven, the Alfvén energy fraction is dominant and therefore it is natural that Alfvénic “signature” overwhelms that of the compressible one. Similarly, the correlation function anisotropy for the A1 MHD cube with the total field in the right panel of Fig.6 is presided over by the correlation function of the pure compressible mode, as seen in the lower panel of Fig.2. It motivates us to evaluate the relative anisotropies as a Y-parameter for the total field in these MHD turbulence cubes. We calculated the Y-parameter from the turbulence data cubes with varying inclination angles of the total field and plotted them in Fig.7. It is clear from this figure that the Y-parameter for these cubes follows the trend of $Y > 1.5$ for Alfvén mode dominance (Z12) and $Y < 1.5$ for compressible mode dominance (A1). We conducted a thorough analysis of the Y-parameter’s behavior by examining all of our MHD cubes. We then created a heatmap of the Y-parameter against θ_λ in ascending order of f_C , which is shown in Fig. 8. We observed that all these cubes maintained their respective trend depending on the mode energy fraction. To avoid ambiguity in the Y-parameter due to approximate similar mode energy fraction, we excluded 5 datacubes from our simulation sets with f_C falling between 0.5 and 0.6. The rest of the total B-field analysis is with the remaining 20 data cubes where

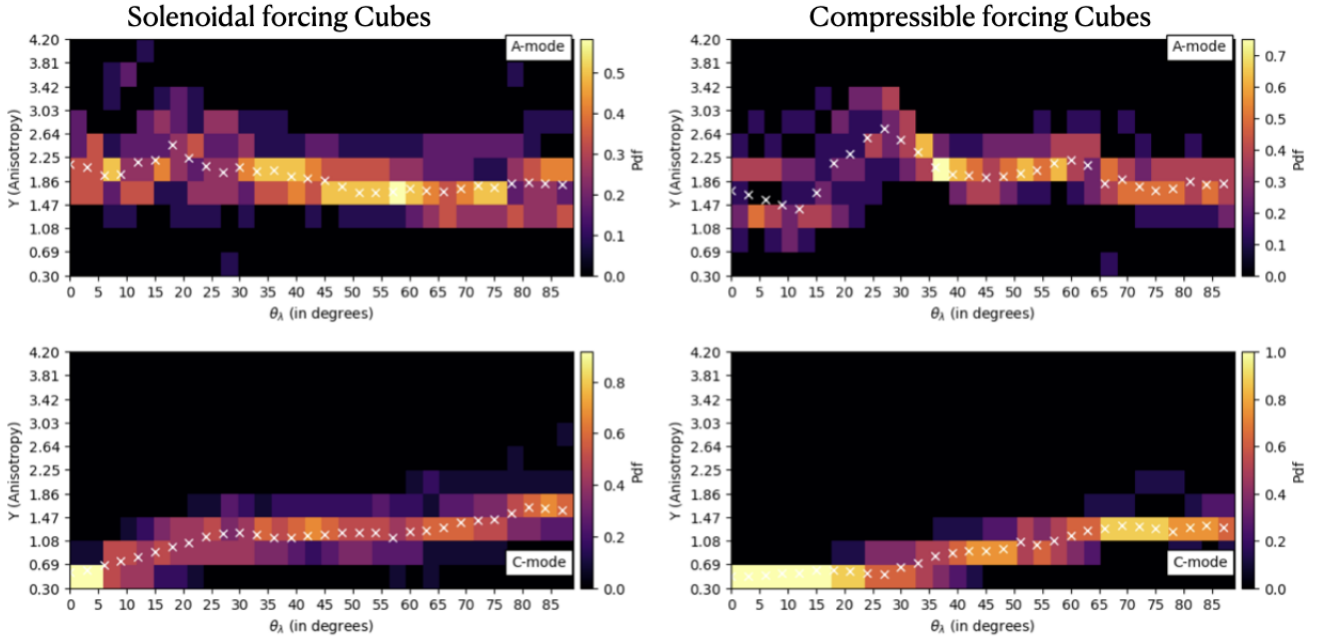


Figure 5. *Left Panel:* To enhance the statistics of the Y-parameter for mode-decomposition, in this plot, we show the probability density and median Y-parameter for the decomposed \mathbf{B} field against the inclination angle of total mean-field, θ_λ . We have taken the median and variance of the Y-parameter for 12 MHD turbulence cubes with $f_c < 0.4$ (see Table 1 for more details). The black color represents the vacancy of data points and hence probability is zero. The color bar represents the PDF at every value of θ_λ . The upper and lower sub-panels are for purely Alfvénic and Compressible modes, respectively. The white cross indicates the median values of the Y-parameter. *Right Panel:* It is the same as the left panel except for MHD cubes. Here we have taken 8 MHD turbulence cubes with C-modes dominance.

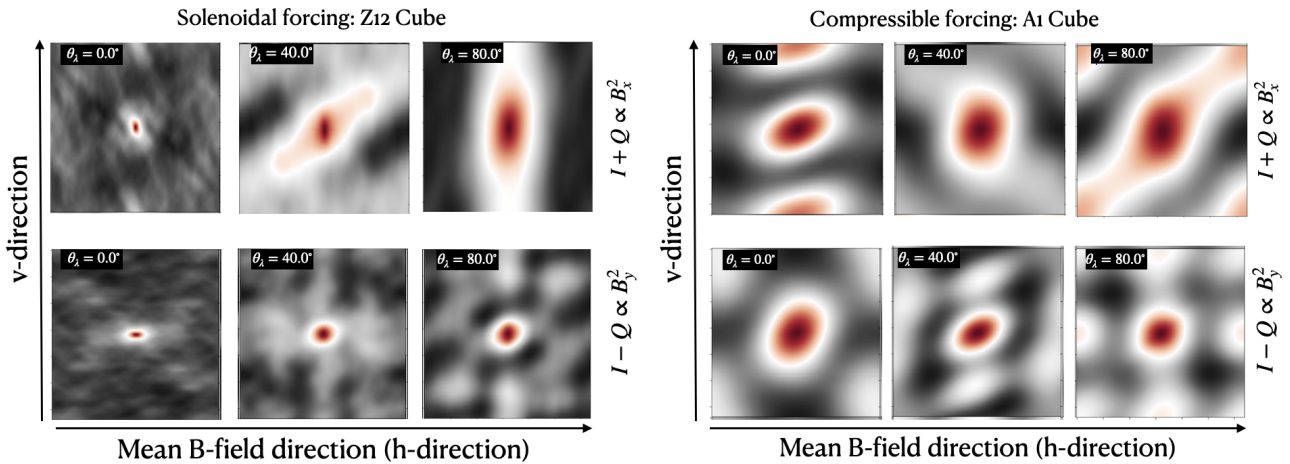


Figure 6. *Left panel:* The figure shows the correlation function of the plane of sky components of the total \mathbf{B} field for the solenoidal forcing Z12 MHD data cubes with $M_A \sim 0.26$ and $\beta \sim 0.12$ at $\theta_\lambda \sim 0.0^\circ, 40.0^\circ, 80.0^\circ$. The upper and lower panel is for B_x^2 and B_y^2 , respectively. *Right panel:* This is the same as the left panel but for the compressible-forcing A1 MHD cube.

12 datacubes have $f_c < 0.4$ and 8 datacubes with $f_c > 0.5$ with $M_A < 1.0$.

Moreover, to strengthen the statistical confidence of the Y-parameter as a diagnostic for 3D magnetic field and MHD turbulence mode, we evaluated the probability density (PDF) and median of the Y-parameter at every value of θ_λ . The PDF and median Y-parameter are shown in Fig. 9, and they follow the respective decomposed mode trends. It indicates that the Y-parameter can serve as an important tool for understanding the 3D magnetic field structures and underlying MHD turbulence in a region.

As a result, from Fig. 9, we can conclude the following inferences for θ_λ :

- If $Y \gtrsim 2.5$, we have $10^\circ < \theta_\lambda < 30^\circ$ and Alfvén dominance i.e. $f_c < 0.4$.
- If $Y \lesssim 1.0$ there are two possibilities: (i) θ_λ is $\lesssim 5^\circ$ and turbulence has C modes dominance i.e. $f_c > 0.5$ (ii) θ_λ is $\gtrsim 60^\circ$ and turbulence is dominated by A-mode.
- $60^\circ \gtrsim \theta_\lambda \gtrsim 40^\circ$ and turbulence is Alfvénic or θ_λ is $\gtrsim 70^\circ$ and the turbulence is compressible if Y-parameter is in the intermediate range;

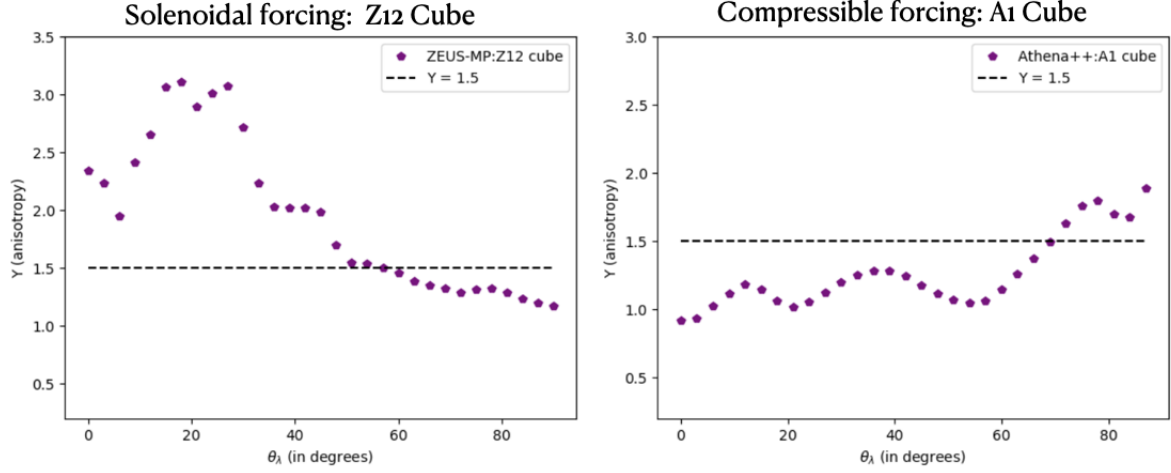


Figure 7. *Left Panel:* The plot of the Y-parameter for the total \mathbf{B} field for the Z12 MHD cube with θ_λ . The black dashed line represents the threshold value of $Y = 1.5$. *Right Panel:* This plot is the same as the left panel but for the A1 MHD cube.

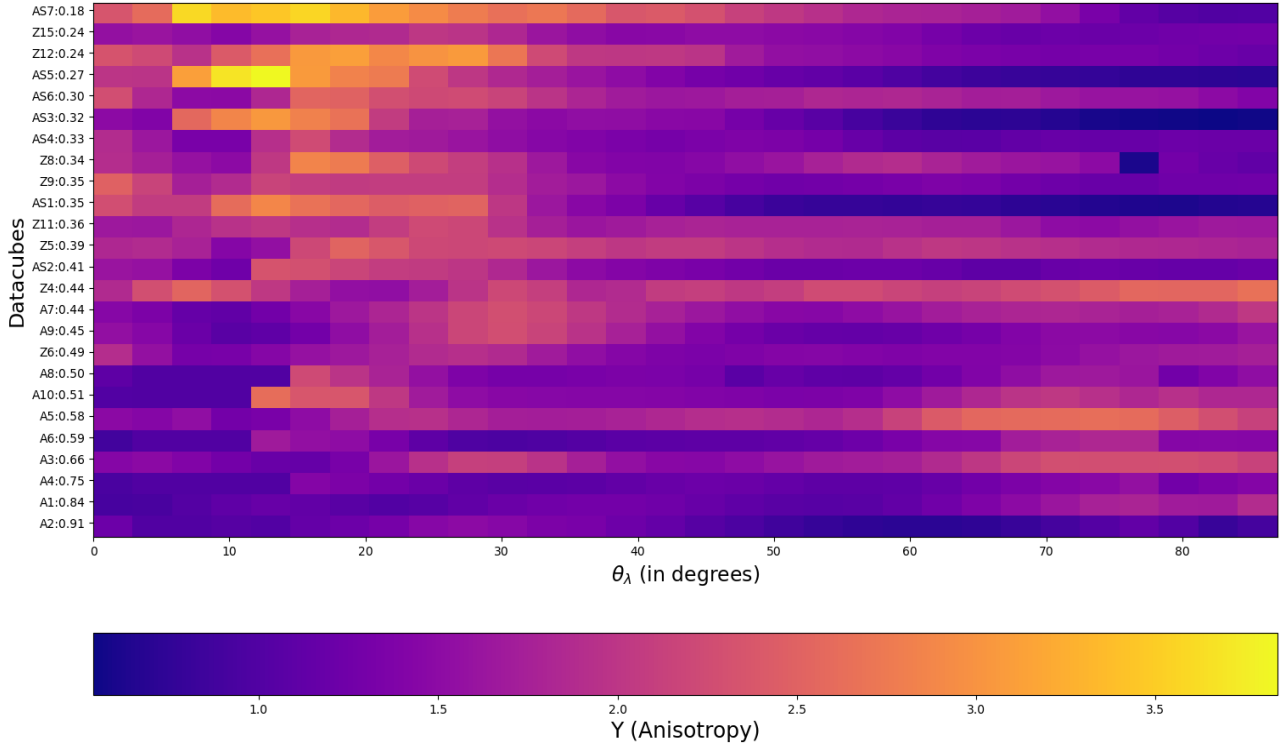


Figure 8. The heatmap shows the distribution of the Y-parameter for 25 MHD datacubes. Here x and y-axes represent the θ_λ and different data cubes sorted in descending order of f_c , respectively.

We have also elaborated our scheme for estimating the magnetic field inclination angle and identifying the dominant MHD turbulence mode in the flowchart shown in Fig 10. It is important to note that the medium's rotation measure influences this technique's applicability. In the case of MHD turbulence simulated datacubes, we have observed that this technique effectively determines the θ_λ values in regions where the emitting layer Faraday rotation and its variance remains within a range of 50° .

From the above discussion, it is clear that the observed statistics of MHD turbulence modes depend on the region's mean magnetic field orientation. As a result, this can be a crucial diagnostics to in-

vestigate the 3D magnetic field in the ISM and extended objects such as SNR and PWN.

5 DISCUSSION

5.1 Implication to general studies of ISM magnetic field and turbulence

Our paper extends the formalism of the two-point studies in synchrotron analysis (see, e.g. Lazarian & Pogosyan 2012). The rela-

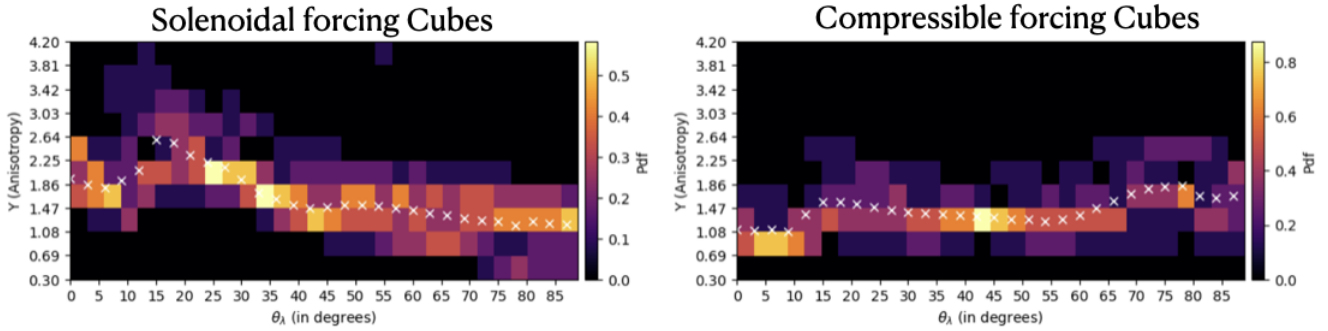


Figure 9. *Left panel:* The plot shows the probability density and median Y-parameter for the PoS total \mathbf{B} field against the θ_λ . We have used 12 MHD cubes with $f_C < 0.4$ with Alfvén modes dominance. The black color represents the vacancy of data points; hence, the probability is zero. The color bar represents the PDF at every value of θ_λ . The white cross indicates the median values of the Y-parameter. *Right Panel:* The plot shows the probability density and median Y-parameter versus θ_λ for the 8 MHD turbulence cubes with C-modes dominance ($f_C > 0.5$).

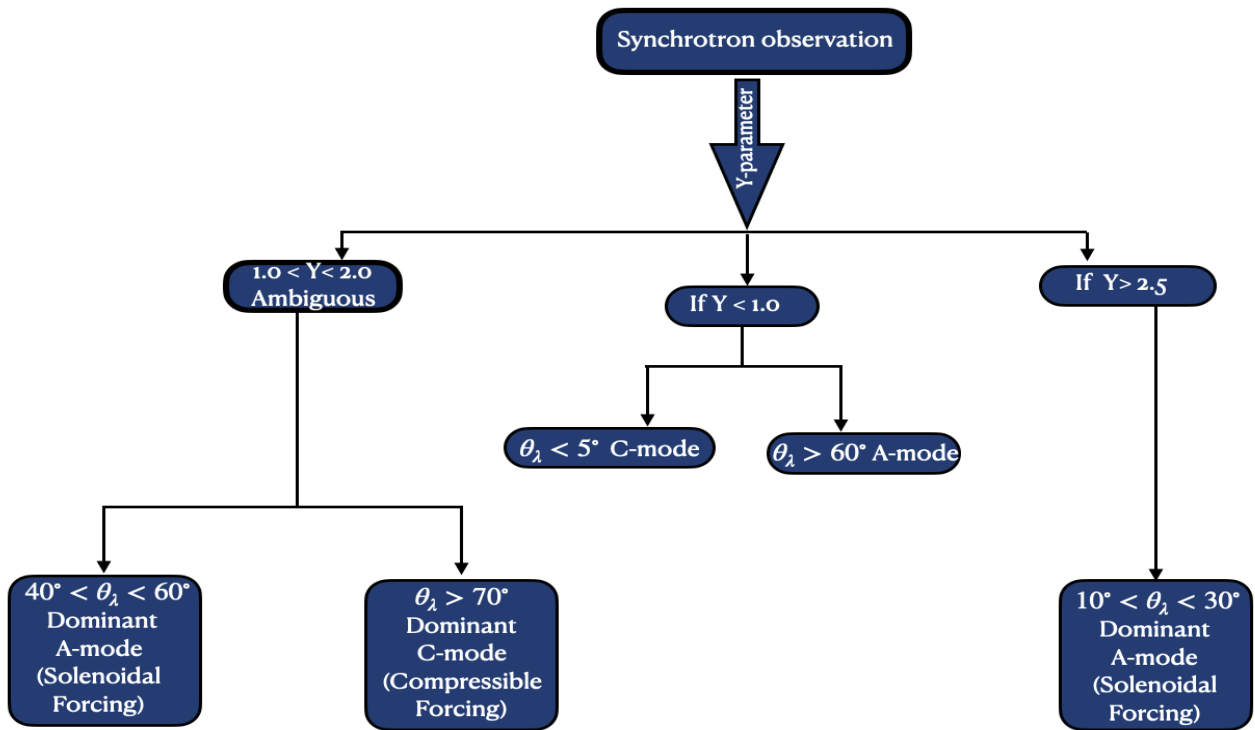


Figure 10. Flowchart to elaborate the scheme for estimating mean field inclination angle and identification of dominant turbulence mode. Here A and C represent the Alfvén and Compressible modes.

relationship between the statistics of various observables and the intrinsic statistics of 3D MHD turbulence variables is a complex and ongoing question within the ISM community (Armstrong et al. 1995; Elmegreen & Scalo 2004; Boldyrev 2006; McKee & Ostriker 2007; Draine 2011). It is mainly due to the absence of true sampling of 3D data like the solar wind community (see, e.g. Zhao et al. 2021, 2022, 2023) and the complications of line-of-sight projections (See, e.g. the same problem for velocity variables, Lazarian & Pogosyan 2000; Yuen et al. 2021). Only in very rare circumstances one can obtain measurements of 3D information in observations, for instance, ground state alignment (Landi Degl’Innocenti & Landolfi 2004; Yan & Lazarian 2006; Kuhn et al. 2007; Yan & Lazarian 2007, 2008b, 2012; Zhang et al. 2020b), dust estimation (Davis & Greenstein 1951; Hildebrand 2002; Lazarian & Hoang 2007; Andersson et al.

2015; Hensley et al. 2019; Zucker et al. 2020) or starlight polarization from GAIA³. These measurements, unfortunately, are sparsely measured to date, which needs to be revised for analysis of the properties of interstellar media (See some attempts in ISM like Seta et al. 2023). Techniques that allow retrieval of intrinsic turbulence properties in ISM is therefore of great importance (e.g. VCS, Lazarian & Pogosyan (2000)).

More recently, the ISM community has developed a few ways of obtaining the turbulence parameters in synchrotron observations, namely sonic Mach number (Gaensler et al. 2011; Burkhart & Lazarian 2012), Alfvénic Mach number (Lazarian et al. 2018), turbulence

³ <https://gea.esac.esa.int/archive/>

index (Lazarian & Pogosyan 2016; Seta et al. 2023) and mode signatures (Zhang et al. 2020a). The remaining puzzles regarding the search of turbulence properties are (i) the relative orientation of the magnetic field angle to the line of sight; (ii) the dependence of energy modes composition diagnosis on the magnetic field inclination angle. Based on the qualitative study of Yuen et al. (2023), in this paper, we have presented a statistical technique to recover the LOS inclination angle θ_λ of the magnetic field with various turbulence parameters, which is important for studies of magnetic field geometry and relevant sciences that depend on the magnetic field orientation.

5.2 Application to ongoing and upcoming radio survey

Radio surveys such as the Low-Frequency Array (LOFAR)⁴, and Square Kilometer Array (SKA)⁵ are currently underway or planned for the near future, promising high-resolution and high-sensitivity radio observations of the interstellar medium (ISM) and galaxies (Gitti et al. 2018). However, current diagnostic techniques are limited to Faraday rotation and polarization measurements of synchrotron emission (Van Eck et al. 2019; Basu et al. 2019; Heald et al. 2020; O’Sullivan et al. 2023), which are sensitive to different components of magnetic fields and are affected by the line-integrated effect. Therefore, there is a pressing need to develop new diagnostic techniques. Our work proposes a well-suited technique for diffuse radio observations from these surveys (Van Eck et al. 2019; O’Sullivan et al. 2023). By analyzing the relative anisotropies involved in observable Stoke parameters, our technique can determine magnetic field orientation and complement the estimation of magnetic field geometry using Faraday rotation, leading to more accurate estimates of the strength and the 3D inclination of the B-field in the ISM.

It is important to note that this technique is designed for the length scales within the inertial ranges. In the case of ISM and any extended sources such as PWN and SNRs, the injection length scales of the turbulence can vary from 50 – 150 pc, thus the required anisotropy for the Y-parameter analysis can be readily captured at scales 5 – 10 pc according to the scale separations in our synthetic observations. The coherence length should be first identified from observations using the well-known structure/correlation function. One such application is discussed briefly in 5.3. Additionally, our analysis enables systematic investigation of the composition of MHD turbulence modes in different plasma environments.

5.3 Implication to observations of Pulsar TeV’s halo

To ensure the reliability of our analysis to investigate the mean field inclination angle and turbulence mode classification, we have applied this technique to archival radio polarisation observations from the $5^\circ \times 5^\circ$ region of Pulsar Wind Nebulae. The radio observations were conducted using the Effelsberg 100-m telescope at a wavelength of 21cm with the resolution of 9.5 arcmin (Uyaniker et al. 1999). Our detailed analysis of this region will be presented in an upcoming publication (Malik et al. 2023).

In brief, this region encompasses the Monogem Pulsar, also known as pulsar B0656+14. Recent observations by the High-Altitude Water Cherenkov Observatory (HAWC) have revealed a

spherical TeV halo around both the Monogem and Geminga pulsars (Abeyssekara et al. 2017). To explain the origin of such high-energy emission, Liu et al. (2019) proposed a model involving an anisotropic diffusion model to explain the TeV observations from the Geminga source. One of the crucial parameters for their analysis is the mean magnetic field inclination angle of the region.

We applied our analysis to the radio polarisation observations to estimate the mean field inclination angle for the Monogem region and found that the Y-parameter is below the 1.5 range. It suggests that the region has primarily *compressible* turbulence, with a low mean-field inclination angle. These outcomes are consistent with theoretical predictions for such a halo from Liu et al. (2019).

5.4 Impact of our work on the studies of magnetic field strength via DCF

Obtaining the value of θ_λ also allows us to determine the magnetic field strength more accurately. The recent debate about the validity of the Davis-Chandrasekhar & Fermi technique (1951; 1953) suggests that the DCF technique is inaccurate in estimating magnetic field strength, with errors up to 1000 times (Skalidis & Tassis 2021). The call for revision of the DCF technique is urgent as most B-field strength estimation in ISM and molecular cloud studies are done by the DCF technique (see, e.g. Liu et al. 2022 for a review). The correction of the DCF technique requires extra turbulence information from interstellar media: Alfvénic Mach number, mode fraction, and line of sight angle, spatial co-existence of dust and spectral line origins (Lazarian et al. 2022; Pavaskar et al. 2023). Our work complements the series of works on correcting the DCF technique in obtaining the true B-field strength in the sky.

6 CONCLUSION

In summary, we have developed a novel diagnostic technique to investigate three-dimensional magnetic fields and underlying MHD turbulence in the ISM. Our technique is primarily based on polarisation observations of the ISM and represents a significant advancement in the field, as no similar diagnostic exists to date. To validate the efficacy of our technique, we tested it extensively using simulated MHD turbulence data cubes with varying plasma properties, energy injection rates, and driving mechanisms (solenoidal or compressible forcing). These simulations also included differences in the composition of Alfvén and Compressible modes. Our results show that our technique can successfully retrieve the mean-field inclination angle, θ_λ , along the line of sight and the underlying dominant MHD turbulence mode. Our major findings are listed below;

- If $Y \gtrsim 2.5$, we have $10^\circ < \theta_\lambda < 30^\circ$ and Alfvén dominance i.e. $f_C < 0.4$.
- If $Y \lesssim 1.0$ there are two possibilities: (i) θ_λ is $\lesssim 5^\circ$ and turbulence is compressible (i.e. $f_C > 0.5$) (ii) θ_λ is $\gtrsim 60^\circ$ and turbulence has A-mode dominance.
- $60^\circ \gtrsim \theta_\lambda \gtrsim 40^\circ$ and turbulence is Alfvénic or θ_λ is $\gtrsim 70^\circ$, and the turbulence is compressible if Y-parameter is in the intermediate range 1.5 ± 0.5 ;
- We found a statistical demarcation of $Y \sim 1.5 \pm 0.5$ (with $Y > 1.5$ for A mode and $Y < 1.5$ for C-mode) to obtain the dominant fraction of MHD turbulence modes.

Hence, our method offers a notable progression in interstellar research, permitting a more detailed exploration of 3D magnetic fields

⁴ <https://lofar-surveys.org/index.html>

⁵ <https://www.skao.int/en>

and MHD turbulence. It effectively reveals valuable insights into ISM turbulence.

ACKNOWLEDGMENTS

We thank the anonymous referee for valuable comments that significantly improved the paper. SM would like to thank P. Pavaskar and SQ Zhao for the helpful discussions. SM and HY gratefully acknowledge the computing time granted by the Resource Allocation Board and provided on the supercomputer Lise and Emmy at NHR@ZIB and NHR@Göttingen as part of the NHR infrastructure. The calculations for this research were conducted with computing resources under the project bbp00062. The research presented in this article was supported by the Laboratory Directed Research and Development program of Los Alamos National Laboratory under project number(s) 20220700PRD1. This research used resources provided by the Los Alamos National Laboratory Institutional Computing Program, which is supported by the U.S. Department of Energy National Nuclear Security Administration under Contract No. 89233218CNA000001. This research also used resources of the National Energy Research Scientific Computing Center (NERSC), a U.S. Department of Energy Office of Science User Facility located at Lawrence Berkeley National Laboratory, operated under Contract No. DE-AC02-05CH11231 using NERSC award FES-ERCAP-m4239 (PI: KHY, LANL).

DATA AVAILABILITY

The MHD turbulence datacubes simulated in this paper are available upon reasonable request from the corresponding author.

REFERENCES

- Abeyssekara A. U., et al., 2017, *Science*, **358**, 911
- Andersson B. G., Lazarian A., Vaillancourt J. E., 2015, *ARA&A*, **53**, 501
- Armstrong J. W., Rickett B. J., Spangler S. R., 1995, *ApJ*, **443**, 209
- Banerjee S., Galtier S., 2013, *Phys. Rev. E*, **87**, 013019
- Basu A., Fletcher A., Mao S. A., Burkhart B., Beck R., Schnitzeler D., 2019, *Galaxies*, **7**, 89
- Boldyrev S., 2006, *Phys. Rev. Lett.*, **96**, 115002
- Burkhart B., Lazarian A., 2012, *ApJ*, **755**, L19
- Chandrasekhar S., Fermi E., 1953, *ApJ*, **118**, 113
- Chepurnov A., Lazarian A., 2010, *ApJ*, **710**, 853
- Chepurnov A., Lazarian A., Stanimirović S., Heiles C., Peek J. E. G., 2010, *ApJ*, **714**, 1398
- Cho J., Lazarian A., 2002, *Phys. Rev. Lett.*, **88**, 245001
- Cho J., Lazarian A., 2003, *MNRAS*, **345**, 325
- Clark S. E., 2018, *ApJ*, **857**, L10
- Crutcher R. M., 1999, *ApJ*, **520**, 706
- Davis L., 1951, *Physical Review*, **81**, 890
- Davis Leverett J., Greenstein J. L., 1951, *ApJ*, **114**, 206
- Draine B. T., 2011, *Physics of the Interstellar and Intergalactic Medium*
- Elmegreen B. G., Scalo J., 2004, *ARA&A*, **42**, 211
- Esquivel A., Lazarian A., 2005, *ApJ*, **631**, 320
- Gaensler B. M., et al., 2011, *Nature*, **478**, 214
- Galtier S., 2009, *ApJ*, **704**, 1371
- Gitti M., Brunetti G., Cassano R., Etori S., 2018, *A&A*, **617**, A11
- Haugen N. E. L., Brandenburg A., Dobler W., 2004, *Phys. Rev. E*, **70**, 016308
- Hayes J. C., Norman M. L., Fiedler R. A., Bordner J. O., Li P. S., Clark S. E., ud-Doula A., Mac Low M.-M., 2006, *ApJS*, **165**, 188
- Heald G., et al., 2020, *Galaxies*, **8**, 53
- Hensley B. S., Zhang C., Bock J. J., 2019, *ApJ*, **887**, 159
- Heyer M., Gong H., Ostriker E., Brunt C., 2008, *ApJ*, **680**, 420
- Hildebrand R. H., 2002, in Trujillo-Bueno J., Moreno-Inseris F., Sánchez F., eds, *Astrophysical Spectropolarimetry*, pp 265–302
- Jokipii J. R., 1966, *ApJ*, **146**, 480
- Kandel D., Lazarian A., Pogosyan D., 2016, *MNRAS*, **461**, 1227
- Kandel D., Lazarian A., Pogosyan D., 2017, *MNRAS*, **464**, 3617
- Kuhn J. R., Berdyugina S. V., Fluri D. M., Harrington D. M., Stenflo J. O., 2007, *ApJ*, **668**, L63
- Landi Degl’Innocenti E., Landolfi M., 2004, *Polarization in Spectral Lines*. Vol. 307, doi:10.1007/978-1-4020-2415-3,
- Lazarian A., Hoang T., 2007, *MNRAS*, **378**, 910
- Lazarian A., Pogosyan D., 2000, *ApJ*, **537**, 720
- Lazarian A., Pogosyan D., 2012, *ApJ*, **747**, 5
- Lazarian A., Pogosyan D., 2016, *ApJ*, **818**, 178
- Lazarian A., Vishniac E. T., Cho J., 2004, *ApJ*, **603**, 180
- Lazarian A., Yuen K. H., Lee H., Cho J., 2017, *ApJ*, **842**, 30
- Lazarian A., Yuen K. H., Ho K. W., Chen J., Lazarian V., Lu Z., Yang B., Hu Y., 2018, *ApJ*, **865**, 46
- Lazarian A., Eyink G. L., Jafari A., Kowal G., Li H., Xu S., Vishniac E. T., 2020, *Physics of Plasmas*, **27**, 012305
- Lazarian A., Yuen K. H., Pogosyan D., 2022, *ApJ*, accepted for publication, p. arXiv: 2204.09731
- Lemoine M., 2022, *Phys. Rev. Lett.*, **129**, 215101
- Lerche I., Schlickeiser R., 2001, *A&A*, **378**, 279
- Liu R.-Y., Yan H., Zhang H., 2019, *Phys. Rev. Lett.*, **123**, 221103
- Liu J., Zhang Q., Qiu K., 2022, *Frontiers in Astronomy and Space Sciences*, **9**, 943556
- Makwana K. D., Yan H., 2020, *Physical Review X*, **10**, 031021
- Malik S., Chand H., Seshadri T. R., 2020, *ApJ*, **890**, 132
- Malik S., K.H. Y., Yan H., 2023, in preparation
- McKee C. F., Ostriker E. C., 2007, *ARA&A*, **45**, 565
- Monin A. S., I’Aglom A. M., 1971, *Statistical fluid mechanics; mechanics of turbulence*
- Müller W.-C., Grappin R., 2005, *Phys. Rev. Lett.*, **95**, 114502
- O’Sullivan S. P., et al., 2023, *MNRAS*, **519**, 5723
- Pavaskar P., Yan H., Cho J., 2023, *Monthly Notices of the Royal Astronomical Society*, **523**, 1056
- Qin G., Mattheus W. H., Bieber J. W., 2002, *ApJ*, **578**, L117
- Sampson M. L., Beattie J. R., Krumholz M. R., Crocker R. M., Federrath C., Seta A., 2023, *MNRAS*, **519**, 1503
- Seta A., Federrath C., Livingston J. D., McClure-Griffiths N. M., 2023, *MNRAS*, **518**, 919
- Shivamoggi B. K., 1999, *Annals of Physics*, **272**, 167
- Skalidis R., Tassis K., 2021, *A&A*, **647**, A186
- Stone J. M., Tomida K., White C. J., Felker K. G., 2020, *ApJS*, **249**, 4
- Uyaniker B., Fürst E., Reich W., Reich P., Wielebinski R., 1999, *A&AS*, **138**, 31
- Van Eck C. L., et al., 2019, *A&A*, **623**, A71
- Verdini A., Grappin R., Hellinger P., Landi S., Müller W. C., 2015, *ApJ*, **804**, 119
- Yan H., 2022, in 37th International Cosmic Ray Conference. p. 38 (arXiv:2109.07847), doi:10.22323/1.395.0038
- Yan H., Lazarian A., 2002, *Phys. Rev. Lett.*, **89**, 281102
- Yan H., Lazarian A., 2004, *ApJ*, **614**, 757
- Yan H., Lazarian A., 2006, *ApJ*, **653**, 1292
- Yan H., Lazarian A., 2007, *ApJ*, **657**, 618
- Yan H., Lazarian A., 2008a, *Astrophys. J.*, **673**, 942
- Yan H., Lazarian A., 2008b, *ApJ*, **677**, 1401
- Yan H., Lazarian A., 2012, *J. Quant. Spectrosc. Radiative Transfer*, **113**, 1409
- Yan H., Lazarian A., Petrosian V., 2008, *Astrophys. J.*, **684**, 1461
- Yuen K. H., Ho K. W., Lazarian A., 2021, *ApJ*, **910**, 161
- Yuen K. H., Yan H., Lazarian A., 2023, *MNRAS*, **521**, 530
- Zhang H., Chepurnov A., Yan H., Makwana K., Santos-Lima R., Appleby S., 2020a, *Nature Astronomy*, **4**, 1001
- Zhang H., Gangi M., Leone F., Taylor A., Yan H., 2020b, *ApJ*, **902**, L7
- Zhao S. Q., Yan H., Liu T. Z., Liu M., Shi M., 2021, *ApJ*, **923**, 253
- Zhao S. Q., Yan H., Liu T. Z., Liu M., Wang H., 2022, *ApJ*, **937**, 102

Zhao S., Yan H., Liu T. Z., Yuen K. H., Wang H., 2023, [arXiv e-prints](#), p. [arXiv:2301.06709](#)

Zucker C., Speagle J. S., Schlafly E. F., Green G. M., Finkbeiner D. P., Goodman A., Alves J., 2020, [A&A](#), **633**, [A51](#)

This paper has been typeset from a \TeX/L\AA\TeX file prepared by the author.